



Research Article

A novel magnetoelastic torque sensor with planar spiral coil probes for humanoid robot joints

Zijian Zhang^a, Zitao Wang^a, Ming Shao^a, Yangyang Dong^{a,*}, Fenglei Ni^b

^a School of Astronautics, Nanjing University of Aeronautics and Astronautics, Nanjing 210016, China

^b State Key Laboratory of Robotics and Systems, Harbin Institute of Technology, Harbin 150001, China

ARTICLE INFO

Article history:

Received 31 August 2024

Revised 15 February 2025

Accepted 17 February 2025

Available online 17 March 2025

Keywords:

Magnetoelastic effect

Torque sensor

Planar spiral coil

Mutual inductance calculation

Hysteresis model

ABSTRACT

Humanoid robot joints require real-time torque detection to provide accurate force feedback information for the control system. To meet the measurement requirements and realize the miniaturization of the sensor, a torque sensor based on the magnetoelastic effect is developed, utilizing planar spiral coils as detection probes. In this work, a planar spiral coil mutual inductance calculation model is established to solve the mutual inductance coefficient, and the mechanical structure and circuit design of the sensor are completed. Finally, a torque loading platform is built to perform calibration experiments, and the hysteresis model is improved to compensate for the hysteresis phenomenon. The calibration results indicate that the sensor shows excellent loaded nonlinearity of 3.08%F.S., unloaded nonlinearity of 2.71%F.S., loaded repeatability of 2.48%F.S., unloaded repeatability of 1.89%F.S. and hysteresis of 1.9%F.S., at a compact probe size of 13.8×9.9×1.8 mm.

© 2025 The Author(s). Published by Elsevier B.V. on behalf of Shandong University. This is an open access article under the CC BY license (<http://creativecommons.org/licenses/by/4.0/>).

1. Introduction

With the development of artificial intelligence and robotics technology, humanoid robot technology has become one of the most cutting-edge fields in current world scientific research [1–3]. Humanoid robots have yet to achieve the intelligent perception and flexible movement abilities that humans possess. To perform more complex, refined, and intelligent tasks, it is essential for robot joints to have force perception capabilities. The torque sensor can sense the magnitude and direction of the torque when the humanoid robot interacts with the operating object and the external environment, providing force sensing information for the compliant control of the humanoid robot [4–6]. Currently, the main torque measurement methods include strain sensors, photoelectric sensors and magnetoelastic sensors [7–9]. Strain type torque sensors have high accuracy and fast response, but the elastic beam structure is complicated and susceptible to external factors [10–12]. Photoelectric torque sensors are highly accurate and simple in structure, but require shaft modification [13–15]. Magnetoelastic torque sensors have the advantages of strong anti-interference ability, simple installation and maintenance, low cost, suitable for online detection, and long working life [16,17]. In summary, strain type and photoelectric torque sensors require the introduction of additional structures such as elastomers and gratings, which can reduce the overall

stiffness of the humanoid robot and affect the motion control system. Magnetoelastic torque sensors can achieve non-contact measurement, and the surrounding arrangement of the probes makes it easier to integrate the sensor into the humanoid robot system.

With the continuous development of soft magnetic alloys and advancements in processing technology, the sensitivity and measurement accuracy of magnetoelastic torque sensors have significantly improved, expanding their potential applications [18]. However, these magnetoelastic torque sensors still have the following drawbacks. Currently, magnetoelastic torque sensors use coupling coils to detect changes in the magnetic permeability of ferromagnetic materials to characterize torque, and usually add iron cores with magnetic permeability to reduce leakage, resulting in an increase in the size and weight of coil probes and sensors, which is not suitable for humanoid robot systems [19]. To achieve miniaturization and integration of magnetoelastic torque sensors and expand their application scenarios, we redesign the coil probe by considering various limiting conditions and manufacturing processes. Finally, the PCB planar spiral octagonal coils are selected as the detection part of the sensor, with the excitation coil and secondary coil located on different layers of the PCB.

2. Measurement principles

The magnetoelastic effect refers to the phenomenon that the magnetic properties of ferromagnetic and sub-ferromagnetic materials change when they are subjected to mechanical stress, also

* Corresponding author.

E-mail address: yy.dong@nuaa.edu.cn (Y. Dong).

known as the inverse magnetostrictive effect [20]. In order to improve the universality of the torque transducer and to avoid the limitation of the material of the test shaft, the measurement is performed by utilizing the magnetoelastic effect of the ferromagnetic material affixed to the test shaft. When subjected to an external excitation magnetic field, ferromagnetic materials with high permeability and low coercivity are prone to magnetization and demagnetization, resulting in narrow hysteresis loops. Meanwhile, magnetostrictive properties should also be considered, so nanocrystalline ribbons were selected as sensitive materials [21–24]. When the torque T_σ is applied to the test shaft with a diameter of D , stress $\pm\sigma = \pm\frac{16T_\sigma}{\pi D^3}$ is generated inside the nanocrystalline ribbons, and the magnetic properties change. Based on the magnetic–mechanical model, a mapping relationship between stress and magnetic induction intensity can be established from the perspective of energy [25]. Therefore, the torque value can be calculated from the output signal of the magnetoelastic torque sensor.

2.1. The relationship between non-hysteresis magnetization and stress

The magnetization state of ferromagnetic materials is altered by changes in the internal magnetic domain structure caused by external magnetic fields or stress. From the macroscopic perspective, the magnetization intensity M generated by changes in magnetic domain structure is equivalent to that generated by an effective magnetic field H_e . The change in the magnetization state caused by the effective magnetic field is equivalent to the combined effect of the external magnetic field and stress. Under constant stress and temperature conditions, the effective magnetic field H_e can be calculated by [26,27]:

$$H_e = H + \alpha M + \frac{3\sigma}{2\mu_0} \frac{d\lambda}{dM} \quad (1)$$

Where α is the molecular field parameter of magnetic moment interaction, $\mu_0 = 4\pi \times \frac{10^{-7}H}{m}$ is the vacuum magnetic permeability, and λ is the magnetostriction coefficient. The third term is generated by the stress, which acts through the magnetostriction coefficient λ . The resulting magnetoelastic effect can be considered equivalent to the influence of an external magnetic field H_σ on the magnetization.

We establish a mathematical model between magnetostriction coefficient λ and stress σ through magnetic domain structure, and establish a relationship between non-hysteresis magnetization intensity M_{an} and stress σ through Langevin function:

$$M_{an} = M_s \left[\coth \left(\frac{H + \alpha M + H_\sigma}{a} \right) - \frac{a}{H + \alpha M + H_\sigma} \right] \quad (2)$$

Where M_s is the saturation magnetization, a characteristic of ferromagnetic materials, M is the magnetization, $a = \frac{N_M k_b T}{\mu_0 M}$ is the intrinsic parameter of the magnetic material, N_M is the number of magnetic domains per unit volume, k_b is the Boltzmann constant, T is temperature.

2.2. The relationship between magnetic induction intensity and stress

The change in magnetization intensity of ferromagnetic materials is not only influenced by external factors such as stress and magnetic field, but also related to the magnetization process. From the model of reversible and irreversible changes in the magnetization process and the effect of elastic energy on the movement of the magnetic domain walls inside the material,

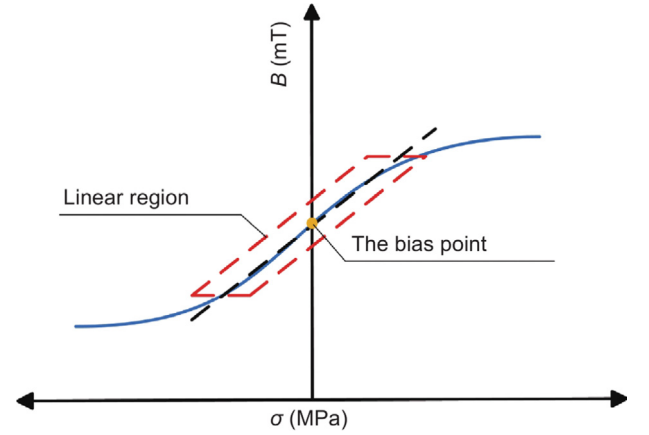


Fig. 1. The approximate linear region of the inverse Magnetoelastic effect.

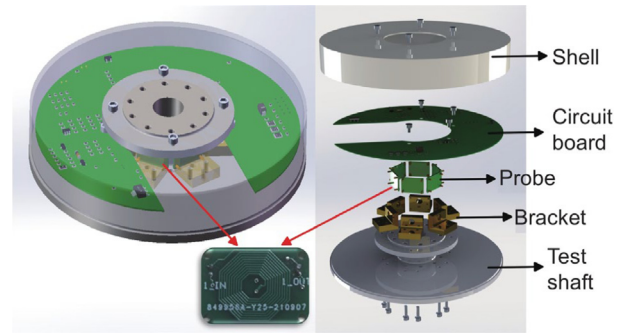


Fig. 2. Structure diagram of the novel magnetoelastic torque sensor.

the relationship between the magnetic induction intensity B and stress σ can be derived as follows [28,29]:

$$\frac{1}{\mu_0} \frac{dB}{d\sigma} = \frac{\sigma}{\varepsilon^2} \left(M_{an} - \frac{B}{\mu_0} + H \right) + c \frac{dM_{an}}{d\sigma} \quad (3)$$

Where ε has the same dimension as stress, and c is the difficulty of magnetic domain wall movement. The curve in Fig. 1 shows that although the relationship between stress and magnetic induction intensity is nonlinear, the stress variation near the material bias point can be approximated as a linear relationship throughout the entire working range of the material.

3. Design of the sensor

As shown in Fig. 2, the torque sensor consists of an elastomeric test shaft, a circuit board, detection probes and nanocrystalline ribbons. The elastomeric test shaft is responsible for transmitting torque. When the test shaft is subjected to torque, the maximum stress is generated at the point with the largest radius. At this time, the nanocrystalline ribbons attached to the surface of the test shaft are subjected to stress, the magnetic permeability changes, and the mutual inductance between the excitation coil and the probe coil changes accordingly. The torque can be characterized by measuring the change in the induced voltage of the probe coil [30].

3.1. Design and optimization of the sensor probe

Although traditional magnetic core coils exhibit low magnetic leakage in the coupling model, their large size and weight increase the motion inertia of the humanoid robot, thereby reducing overall stability. The circular planar spiral coil has a lower

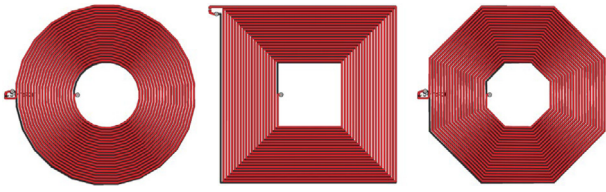


Fig. 3. Circular, rectangular and octagonal planar spiral coils.

area utilization rate and its accuracy is lower than that of the rectangular coil when the probe size is the same. When PCB coils use sharp-angle and right-angle routing, impedance discontinuity will cause signal reflection and result in signal distortion. As shown in Fig. 3, considering volume limitation, precision improvement, electromagnetic compatibility and other factors, the PCB planar spiral octagonal coils are used as the sensor probes [31].

3.1.1. Analytical models

The PCB coil assembly has the advantages of small size and easy installation. However, the number of coil turns is limited, resulting in serious magnetic leakage. Therefore, it is necessary to develop and simulate a PCB coil coupling model while selecting appropriate coil parameters to improve the effective coupling of the coil system.

According to the basic definition of electromagnetics, the mutual inductance coefficient M_u can be expressed as follows [32]:

$$M_u = \frac{\varphi}{I} = \frac{\int \mathbf{B}d\mathbf{S}}{I} \quad (4)$$

Where φ is the magnetic flux of the secondary coil, I is the current in the excitation coil, \mathbf{B} is the magnetic induction intensity of the secondary coil, and \mathbf{S} is the cross-sectional area of the secondary coil. The mutual inductance coefficient M_u needs to be calculated through the magnetic flux φ and the magnetic induction intensity \mathbf{B} .

3.1.2. Calculation of magnetic induction intensity

In Fig. 4, each side of the planar spiral octagonal coil is a straight wire. For a straight wire $A(x_A, y_A, z_A)D(x_D, y_D, z_D)$, the magnetic induction intensity B_p generated by the current element ldz at any point $P(x, y, z)$ in space can be calculated based on the Biot-Savart law and can be expressed as follows:

$$\begin{aligned} B_p &= \frac{\mu_0 I}{4\pi l} \int_{\theta_2}^{\theta_1} \sin \theta d\theta = \frac{\mu_0 I}{4\pi l} (\cos \theta_1 - \cos \theta_2) \\ &= \frac{\mu_0 I}{4\pi l} \left(\frac{\vec{AD} \cdot \vec{AP}}{|\vec{AD}| |\vec{AP}|} - \frac{\vec{AD} \cdot \vec{DP}}{|\vec{AD}| |\vec{DP}|} \right) \end{aligned} \quad (5)$$

Where μ_0 is the magnetic permeability of vacuum, l is the distance from point P to AD , θ is the angle between the current element and the position vector of point P , θ_1 is the angle between AP and AD , θ_2 is the angle between DP and AD , and the direction of the magnetic induction intensity B_p is determined by the right-hand screw rule. This formula calculates the magnetic induction intensity vector, and its component B_{pe} perpendicular to the plane of the receiving coil is required when calculating the mutual inductance coefficient.

$$\begin{aligned} B_{pe} &= B_p \times \sin \theta_v \\ &= \frac{B_p}{|\vec{AD} \times \vec{DP}|} [(x_D - x_A)(y - y_D) - (x - x_D)(y_D - y_A)] \end{aligned} \quad (6)$$

Where θ_v is the angle between the magnetic induction intensity vector and plane XOY .

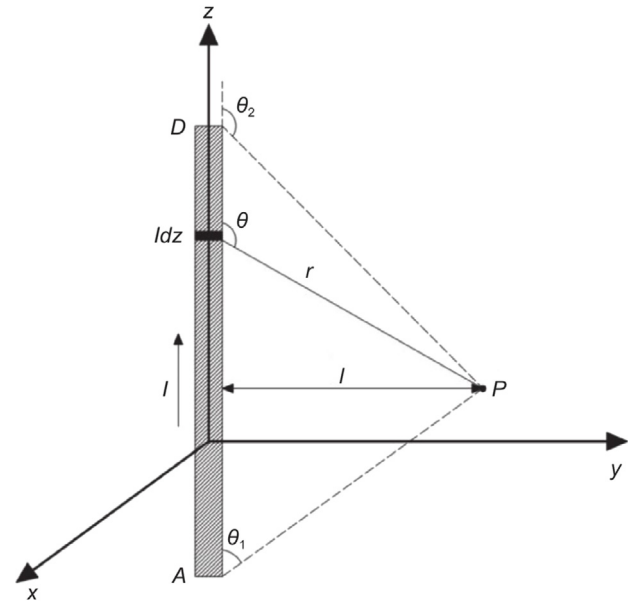


Fig. 4. Biot-Savart law describes the magnetic field generated by a current element at any point P in space.

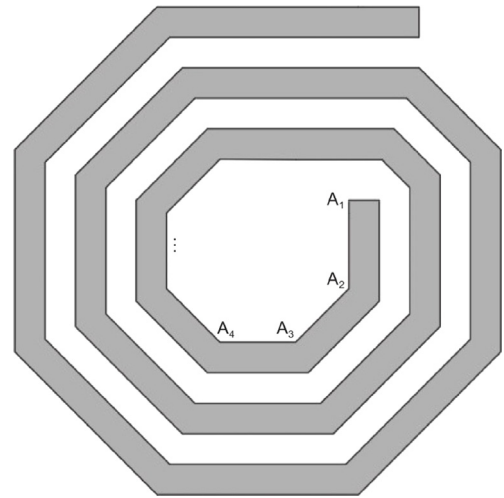


Fig. 5. The vertices of a planar octagonal spiral coil.

3.1.3. Calculation of mutual inductance

From Eq. (5), we can know that the effective magnetic induction intensity generated by a straight wire at a point in space is related to the coordinates of the endpoints of the straight wire. Therefore, it is necessary to determine the vertex coordinates of the planar spiral octagonal coil.

In Fig. 5, the center of the secondary coil is taken as the origin of the coordinates, and the coordinates of the starting point A_1 are given as $(x_1, y_1, 0)$, then the recursive relationship of the coordinates of the vertices of the excitation coil is as follows [33]:

$$\begin{aligned} x_{A_k} &= x_{A_{k-1}} + \left| \vec{A_{k-1}A_k} \right| \cos \theta_{A_{k-1}A_k} \\ y_{A_k} &= y_{A_{k-1}} + \left| \vec{A_{k-1}A_k} \right| \sin \theta_{A_{k-1}A_k} \\ z_{A_k} &= h \end{aligned} \quad (7)$$

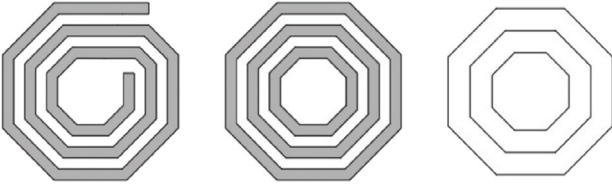


Fig. 6. The coil simplification process for the sake of calculation convenience.

Where $\theta_{A_{k-1}A_k}$ is the angle between the edge vector $\overrightarrow{A_{k-1}A_k}$ and the positive direction of the x -axis, $|\overrightarrow{A_{k-1}A_k}|$ is the length of the coil side, and h is the distance between the excitation coil surface and the secondary coil surface. These parameters are determined by the coil size and experimental conditions, so they can be obtained through measurements in the experiment.

As shown in Fig. 6, to facilitate calculations, the secondary planar spiral octagonal coil model is simplified into a set of concentric single-turn coils. According to the superposition principle, the mutual inductance coefficient M_A between the excitation coil and the secondary coil is equal to the sum of the mutual inductance coefficient M_i between each side of the excitation coil and each single-turn coil of the secondary coil.

$$M_A = \sum_{i=1}^n M_i \quad (8)$$

Where n is the number of turns of the simplified secondary coil, and M_i is the mutual inductance coefficient between the excitation coil and the i -th secondary coil.

For the simplified coil model, when calculating the mutual inductance coefficient of the coupling of two single-turn coils, the integral region contained in each single-turn coil only needs to be divided once. Additionally, the symmetry of the regular octagon can be used to reduce the complexity of the calculation. The integral region division is shown in Fig. 7, where l_2 is the side length of the secondary coil. The integration area is divided into three parts, the total magnetic flux of the secondary coil is the

sum of the magnetic fluxes of the three areas.

$$\phi_1 = \int_{\frac{1}{2}l_2}^{\frac{1+\sqrt{2}}{2}l_2} \int_{x-\frac{2+\sqrt{2}}{2}l_2}^{-x+\frac{2+\sqrt{2}}{2}l_2} (B_1 + B_2 + \dots + B_{k-1}) dx dy$$

$$\phi_2 = \int_{-\frac{1}{2}l_2}^{\frac{1}{2}l_2} \int_{-\frac{1+\sqrt{2}}{2}l_2}^{\frac{1+\sqrt{2}}{2}l_2} (B_1 + B_2 + \dots + B_{k-1}) dx dy \quad (9)$$

$$\phi_3 = \int_{-\frac{1}{2}l_2}^{\frac{1}{2}l_2} \int_{-x-\frac{2+\sqrt{2}}{2}l_2}^{x+\frac{2+\sqrt{2}}{2}l_2} (B_1 + B_2 + \dots + B_{k-1}) dx dy$$

Where ϕ_1, ϕ_2, ϕ_3 are the magnetic fluxes of region 1, region 2, and region 3 respectively, B_1, B_2, \dots, B_{k-1} are the effective magnetic induction intensities generated by each side of the excitation coil in the integral area, and can be calculated using (6)Eq. (6) [34]. The mutual inductance coefficient M_i can be calculated by Eq. (10).

$$M_i = \frac{\phi_1 + \phi_2 + \phi_3}{I} \quad (10)$$

By successively calculating the mutual inductance coefficient between each side of the excitation coil and each single turn of the secondary coil, we can obtain the total mutual inductance coefficient between the excitation coil and the secondary coil. The mutual inductance algorithm proposed in this paper is compared with the simulation results and the mutual inductance calculation algorithm proposed by Hadi [34]. The results are shown in Fig. 8, it is obviously that there is consistency among the three results.

3.1.4. Optimization

According to PCB design rules, increasing the line spacing results in a decrease in the number of turns. As indicated by Eq. (8), when the number of turns in the secondary coil increases, the mutual inductance coefficient correspondingly rises. Once the minimum safe distance for circuit processing is reached, the mutual inductance coefficient of the coil coupling system attains its maximum value. To further improve the quality of coil coupling, the number of layers of the excitation coil and the secondary coil can be increased, and copper layers can be added to shield external electromagnetic interference [35].

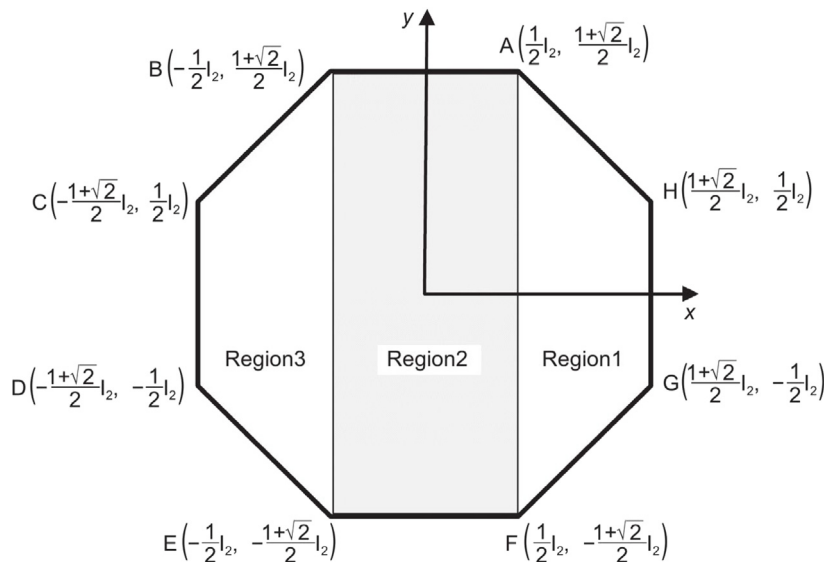


Fig. 7. The result of dividing the integration region using symmetry.

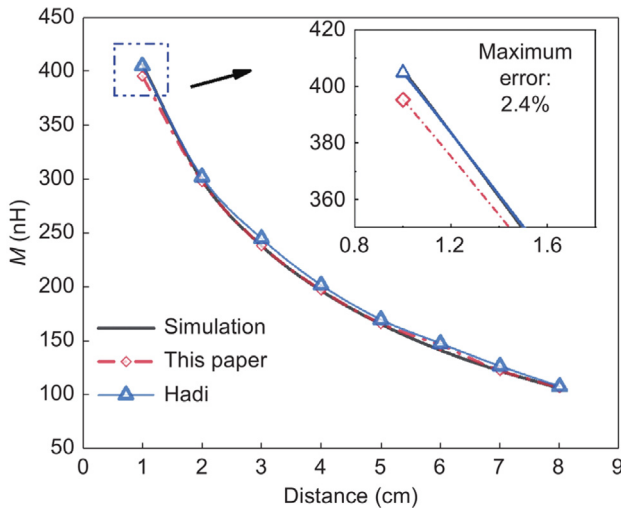


Fig. 8. Comparison between simulation analysis and theoretical calculation.

3.2. Structural simulation

The elastomeric test shaft serves as the supporting structure for the entire system and as the attachment point for the nanocrystalline ribbons. Its mechanical properties are directly related to the sensor accuracy. When conducting equivalent tests on application scenarios of robot joints, a hollow elastomer test shaft is used because the hollow shaft configuration can increase stiffness and leave space for wiring. A mechanical simulation is performed on it, and the results are shown in Fig. 9. When a torque of 100 N m is applied to the test shaft, the surface stress is 36 MPa, the surface strain is 8×10^{-6} , and the converted torsion angle is 0.035° . When connected in series to the robotic arm system, the overall strength of the system can be guaranteed, at the same time, the measurement accuracy can be improved.

3.3. Circuit design

As illustrated in Fig. 10, the sensor circuit includes a signal generation module and a signal collecting module. The signal generation module completes the conversion of the voltage analog quantity to the sinusoidal excitation signal, which is used as the signal input of the excitation coil. Its signal-to-noise ratio and amplitude stability will directly affect the accuracy of the measurement. Therefore, the signal generation circuit uses FPGA as the main control chip and adopts direct digital frequency synthesis technology (DDS) to generate a stable sinusoidal excitation signal with adjustable frequency and amplitude. The signal collecting module collects the analog induced voltage signal of the probe coil, and after passing through the attenuation circuit, attenuates the analog voltage amplitude to the working voltage range of the analog-to-digital conversion chip to complete the analog-to-digital conversion.

4. Experiments and calibration

4.1. Experimental platform

In the experiment, steel wire hooks were used to connect the weight and the torque loading rod, enabling the application of a static torque to the measured axis of the elastic body. A symmetrical design was implemented to prevent uneven force distribution on the measured axis resulting from unilateral loading. As illustrated in Fig. 11, the experimental platform uses a

structure with two sets of rectangular frames superimposed to ensure that the platform surface is parallel to the ground, thereby achieving the loading torque parallel to the measured axis. The frame is made of aluminum alloy, which has little effect on the magnetic field, ensuring the measurement accuracy of the sensor in an alternating magnetic field environment.

4.2. Excitation signal

The excitation signal frequency directly affects the planar spiral coil coupling effect and the magnetic susceptibility of the nanocrystalline ribbons. When the excitation signal frequency is low, the torque sensor outputs a small reference voltage, and the system error accounts for a large proportion of the reference voltage. Since the PCB planar spiral coil has no iron core to concentrate the magnetic field, the coupling effect of the planar spiral coil can only be improved by increasing the excitation signal frequency. When the excitation signal frequency is increased, the output reference voltage increases, and the system error ratio decreases accordingly. However, if the excitation signal frequency is too high, the inverse magnetostrictive material will produce a serious demagnetization field, resulting in inconsistent loading and unloading curves of the sensor output and widening of the hysteresis curve. Therefore, the excitation signal frequency is selected as 5 MHz in the experiment. Increasing the peak-to-peak value of the signal enhances the full-scale output of the sensor. However, as the peak-to-peak value increases, the nanocrystalline ribbons tend to saturate magnetization and the linearity of the sensor output decreases. Therefore, the excitation signal amplitude is selected to be 5 V, that is, the signal peak-to-peak value is 10 Vpp [36].

4.3. Hysteresis compensation

Ferromagnetic materials have hysteresis phenomenon, which causes the sensor to have a hysteresis loop when measuring. In other words, the output value depends on both the current and historical input values. To improve the accuracy of the sensor, hysteresis compensation should be performed [37]. The PI hysteresis model is a phenomenon-based mathematical model that can directly solve the PI hysteresis inverse model through numerical calculations [38]. The classic PI model is obtained by weighted summation of hysteresis operators with different thresholds in Fig. 12, which can be expressed as [39]:

$$y(t) = w^T H_r [u(t), y_0] \\ = \sum_{i=1}^N w_i \cdot \max \{u(t) - r_i, \min [u(t) + r_i, y_i(t - T)]\} \quad (11)$$

Where $w^T = [w_1, w_2, \dots, w_N]^T$ is the weight vector, H_r represents the hysteresis operator with a threshold of r , N is the number of hysteresis operators, $u(t)$ is the input voltage, y_0 is the initial value of the operator, and $y_i(t - T)$ is the output of the operator i at the previous moment. Increasing the number of operators and adjusting the operator threshold can improve the accuracy of the model, but the amount of calculation will also increase.

The Play operator used in the classic PI hysteresis model has central symmetry and cannot describe asymmetric models. In practical applications, the hysteresis curve output by the sensor is offset and not symmetrical. It is necessary to add a polynomial to the classic Play operator to more accurately describe the asymmetric hysteresis loop. The model expression using the improved

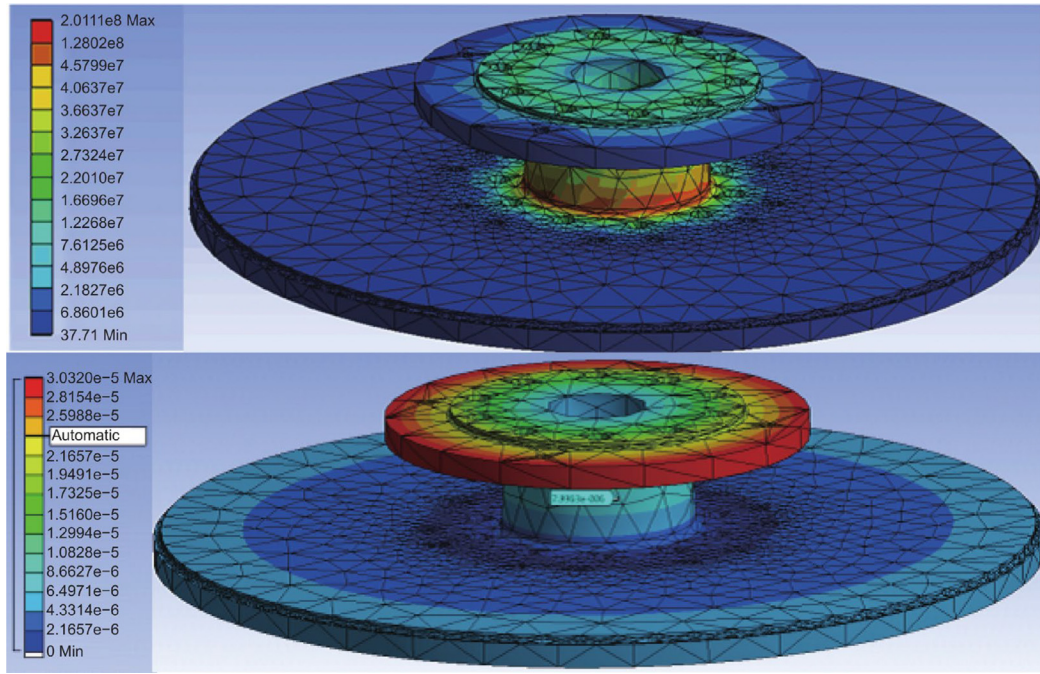


Fig. 9. Simulation results of stress and strain in the elastomeric test shaft.

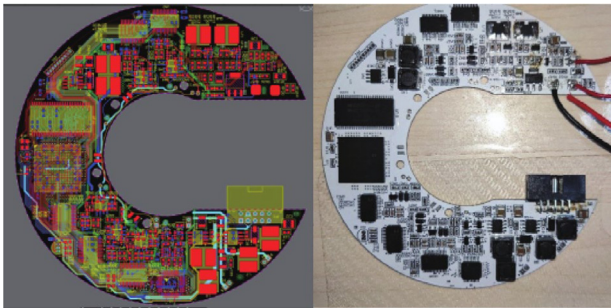


Fig. 10. Circuit design layout and circuit physical diagram.

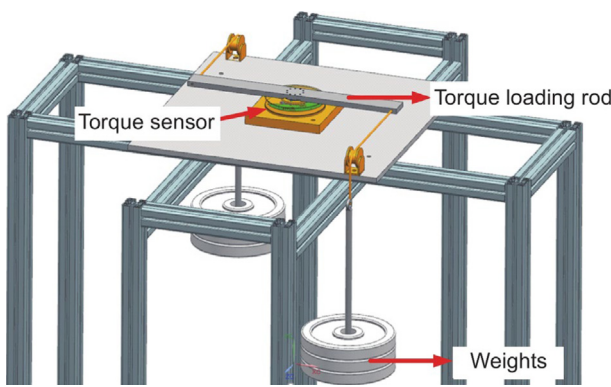


Fig. 11. Torque static loading platform in the experiment.

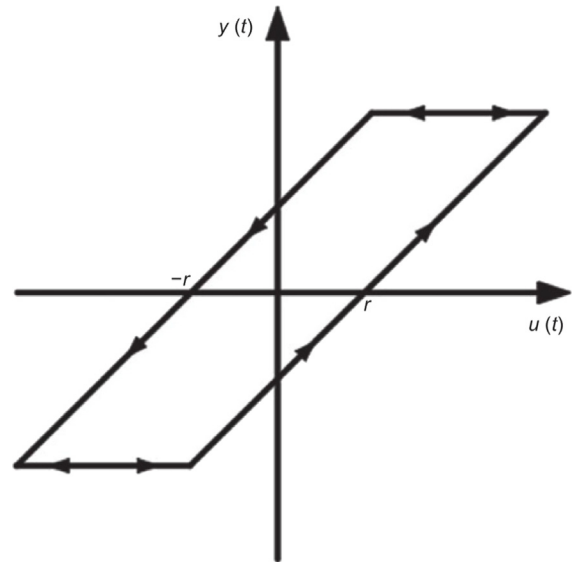


Fig. 12. Play operator of the classic PI hysteresis model.

Play operator is as follows [40]:

$$y_c(t) = g(u(t)) + \sum_{i=1}^N w_i \cdot \max \{u(t) - r_i, \min [u(t) + r_i, y_i(t - T)]\} \quad (12)$$

Where $g(u(t)) = a_1 u^3(t) + a_2 u(t)$, a_1 , a_2 , r_i and w_i are obtained by least squares parameter identification method. For the convenience of identification, the measured dataset is shifted to the extreme value. To improve the fitting accuracy, the dataset is expanded by spline interpolation method.

Fig. 13 shows the compensation principle based on the PI inverse model. In general, the PI model can be established based on experimental data, and then the inverse model can be solved for hysteresis compensation. The form of the PI inverse model is the same as that of the PI model, the only difference is whether the hysteresis curve is counterclockwise or clockwise, so the inverse model can be solved directly [41].

The results obtained by hysteresis compensation are shown in Fig. 14. The hysteresis error of the torque sensor is reduced

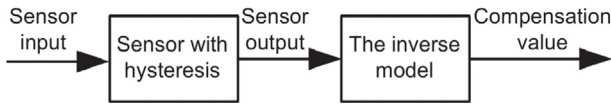


Fig. 13. Compensation principle based on PI inverse model.

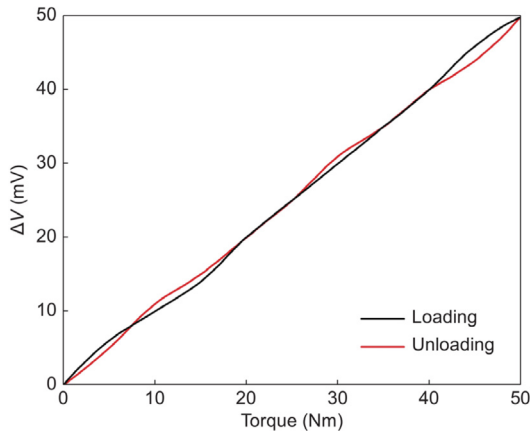


Fig. 14. Sensor output after hysteresis compensation.

from 8.95% to 1.9%. If the number of operators is increased, the hysteresis error can be further reduced. Since the model is based on experimental data, the compensation effect will be affected by the repeatability error of the sensor, so the hysteresis error cannot be completely eliminated.

4.4. Experimental data analysis

In the calibration experiment, torque loading and unloading are achieved by changing the weight of the calibration mass. Due to the anisotropy of the test shaft, sensitive materials are applied to different locations on the surface of the shaft, and Sensor I and Sensor II are placed accordingly. The inductive signal data corresponding to each torque value are recorded and fitted using the least squares method, with the results shown in Fig. 15. The linearity of Sensor I is superior to that of Sensor II. The loading and unloading fitting equations for Sensor I are represented by

$f(x) = -0.002927x + 5.304$ and $f(x) = -0.00283x + 5.299$, the R-Square values are 0.9923 and 0.9943, with nonlinear fitting errors are 3.08% and 2.71%.

According to the measurement principle, the output of the sensor is approximately linear with respect to the input. Therefore, polynomial fitting is performed on the experimental data of Sensor I. As shown in Fig. 16, the accuracy of the cubic polynomial is higher than that of the quadratic polynomial, with the loading and unloading fitting equations are represented by $f(x) = 1.538 \times 10^{-6}x^3 - 1.284 \times 10^{-4}x^2 + 8.298 \times 10^{-5}x + 5.287$ and $f(x) = 7.537 \times 10^{-7}x^3 - 6.657 \times 10^{-5}x^2 - 1.155 \times 10^{-3}x + 5.288$, the R-Square values are 0.9987 and 0.9963, and the fitting errors are 1.28% and 2.03%.

In the repeatability experiment, the torque increment for each change is 5 Nm, with a total range of 50 Nm. Each loading and unloading experiment consists of 11 data points. To ensure the reliability of the experimental data, five sets of comparison tests were conducted at different time intervals, starting from the first set of experimental time, without changing the experimental conditions. The output results of Sensor I and Sensor II are shown in Fig. 17. The overall loaded repeatability error of the sensor is 2.48%, the unloaded repeatability error is 1.89%, and the hysteresis error is 1.9%.

5. Conclusions

In this paper, we present the design of a torque sensor that operates on the magnetoelastic effect. We have selected PCB planar spiral octagonal coils as probes to measure torque by characterizing changes in the magnetic permeability of the magnetic material as variations in voltage amplitude. To optimize the performance of the sensor while minimizing its volume and weight, we established a mathematical model of the mutual inductance of the planar spiral coil, ensuring effective coupling. Additionally, we conducted mechanical simulations of the elastomer shaft, which demonstrated that connecting the sensors in series to the joints of a humanoid robot does not significantly impact system stiffness. Furthermore, we addressed the issue of hysteresis error, successfully reducing it to 1.9% by employing an improved PI hysteresis model for compensation. The proposed torque sensor meets the operational requirements of humanoid robots. However, further improvements are needed in the soft magnetic material pasting process to maintain uniform glue layer thickness and to identify the optimal pasting position for minimizing the influence of the magnetic anisotropy of the sensitive material [42].

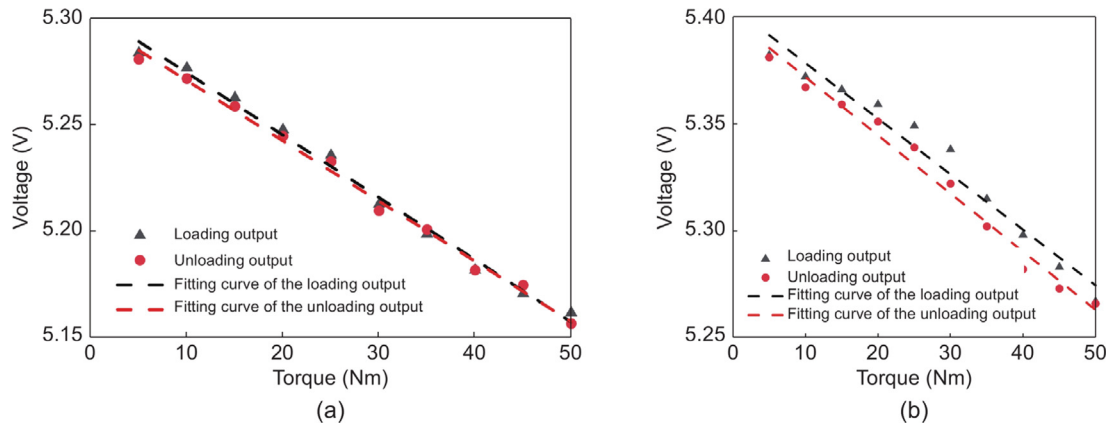


Fig. 15. Results of the calibration experiment. (a) Experimental data and fitting curves of Sensor I. (b) Experimental data and fitting curves of Sensor II.

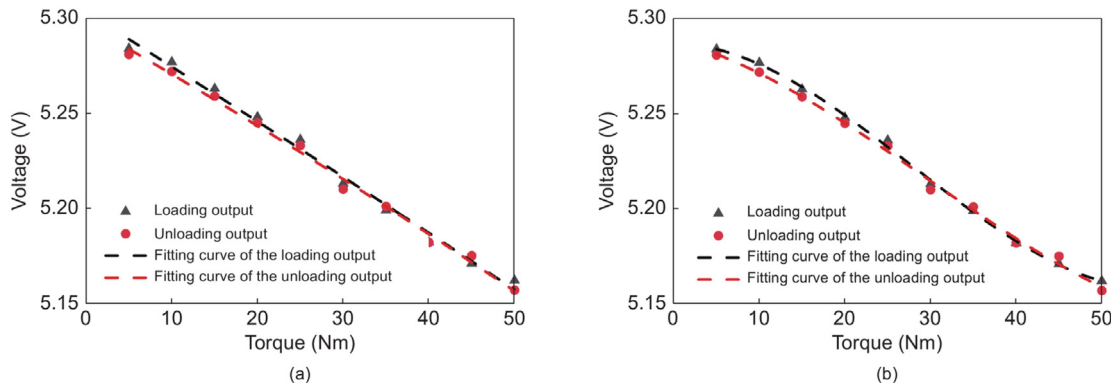


Fig. 16. (a)The quadratic polynomial fitting curve. (b)The cubic polynomial fitting curve.

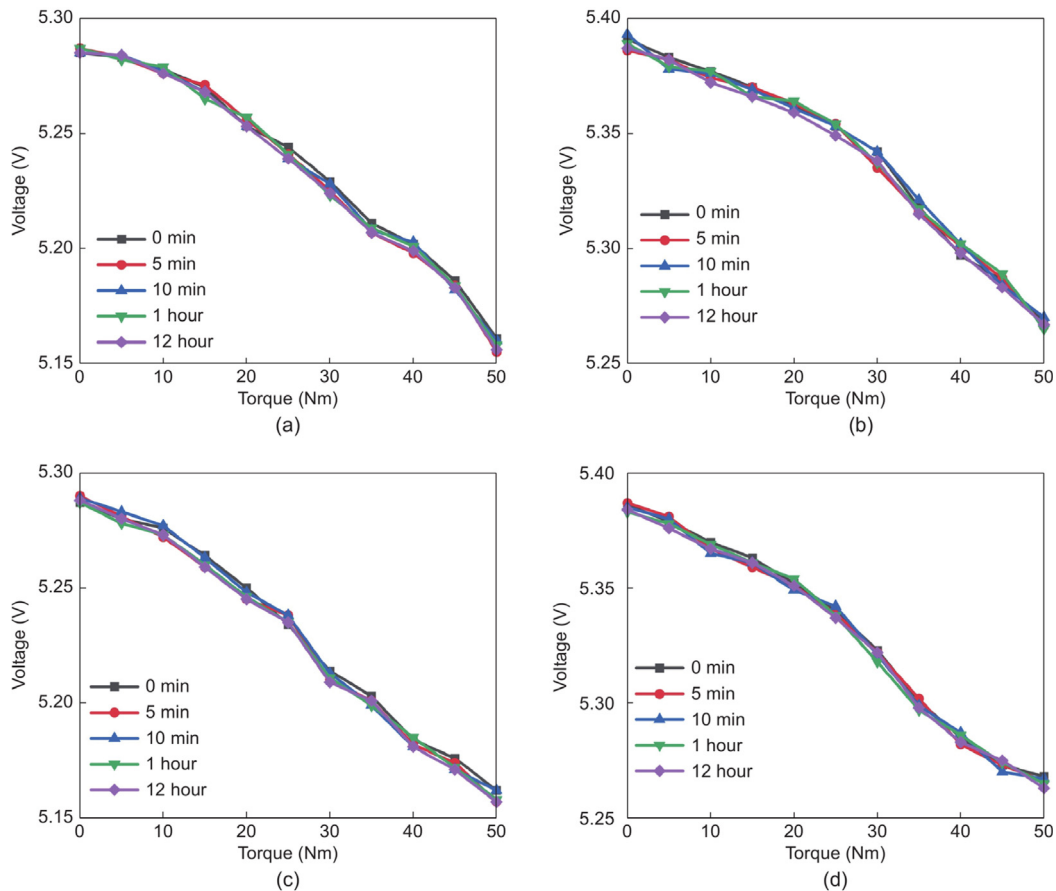


Fig. 17. Results of the repeatability experiment. (a) Loading output curve of sensor I. (b) Loading output curve of sensor II. (c) Unloading output curve of sensor I. (d) Unloading output curve of sensor II.

CRediT authorship contribution statement

Zijian Zhang: Writing – review & editing, Supervision, Methodology. **Zitao Wang:** Writing – original draft. **Ming Shao:** Formal analysis. **Yangyang Dong:** Writing – review & editing, Supervision, Project administration. **Fenglei Ni:** Funding acquisition, Formal analysis.

Declaration of competing interest

The authors declare that they have no known competing financial interests or personal relationships that could have appeared to influence the work reported in this paper.

Acknowledgments

This work is supported in part by Guangxi Science and Technology Program, China (2024AB12006), the Open Fund of Innovation Center for Control Actuators, China (ICCA18-202405) and China Huaneng Group.,Ltd. Headquarters Technology Project (HNKJ24-HF15).

Appendix A. Supplementary data

Supplementary material related to this article can be found online at <https://doi.org/10.1016/j.birob.2025.100229>.

References

- [1] R. Dou, S. Yu, W. Li, et al., Inverse kinematics for a 7-DOF humanoid robotic arm with joint limit and end pose coupling, *Mech. Mach. Theory* 169 (2022) 104637.
- [2] H. Huang, S.Q. Liu, Are consumers more attracted to restaurants featuring humanoid or non-humanoid service robots? *Int. J. Hosp. Manag.* 107 (2022) 103310.
- [3] Y. Li, L. Zhu, Z. Zhang, et al., Humanoid robot heads for human-robot interaction: A review, *Sci. China Technol. Sci.* 67 (2) (2024) 357–379.
- [4] Y. Liu, X. Chen, Z. Yu, et al., High-precision dynamic torque control of high stiffness actuator for humanoids, *ISA Trans.* 141 (2023) 401–413.
- [5] B. Fu, G. Cai, Design and optimization of a joint torque sensor with small crosstalk error for robots, *Measurement* 200 (2022) 111629.
- [6] S.C. Mahadik, V.R. Deulgaonkar, S.M. Bhosle, *Robotic Joint Torque Sensors: A Review*, Cham, Springer International Publishing, 2024.
- [7] L. Shi, J. Feng, Y. Zhu, et al., A review of flexible strain sensors for walking gait monitoring, *Sens. Actuators A: Phys.* 377 (2024) 115730.
- [8] I.J. Garshelis, Torque and power measurement, in: *Mechanical Variables Measurement-Solid, Fluid, and Thermal*, CRC Press, 2023, 5-1-5-16.
- [9] W.J. Fleming, Automotive torque measurement: A summary of seven different methods, in: *Proceedings of the 32nd IEEE Vehicular Technology Conference*, IEEE, 1982.
- [10] Y.-J. Wang, P.-K. Chi, Y.-H. Lin, et al., A six-axis force and torque sensor consisting of compliant mechanisms and full-bridge strain gauges, *Measurement* 226 (2024) 114151.
- [11] M. Pu, J. Zhang, Q. Luo, et al., Theory and application of an optimal design method for capacitive six-axis force/torque sensors, *Measurement* 203 (2022) 112009.
- [12] S. Aiguo, F. Liyue, Multi-dimensional force sensor for haptic interaction: A review, *Virtual Real. Intell. Hardw.* 1 (2) (2019) 121–135.
- [13] S. Zhong, L. Chen, W. Liang, et al., Contactless torque sensors based on optical methods: A review, *Opt. Lasers Eng.* 173 (2024) 107832.
- [14] Z. Li, X. Li, J. Lin, et al., Design and application of multidimensional force/torque sensors in surgical robots: A review, *IEEE Sens. J.* 23 (12) (2023) 12441–12454.
- [15] G. Palli, S. Pirozzi, An optical torque sensor for robotic applications, *Int. J. Optomechatronics* 7 (4) (2013) 263–282.
- [16] S. Mirzamohamadi, M.M. Sheikhi, M.R. Karafi, et al., Novel contactless hybrid static magnetostrictive force-torque (chsmft) sensor using galferol, *J. Magn. Magn. Mater.* 553 (2022) 168969.
- [17] X. Tousignant, D. Ménard, Optimization of magnetoelastic torque meter designs, *IEEE Trans. Magn.* 57 (2) (2020) 1–4.
- [18] Y.-S. Zhan, C.-H. Lin, A constitutive model of coupled magneto-thermo-mechanical hysteresis behavior for giant magnetostrictive materials, *Mech. Mater.* 148 (2020) 103477.
- [19] J. Liu, L. Yang, J. Ma, The state-of-art and prospect of contactless torque measurement methods, in: *Proceedings of the IOP Conference Series: Materials Science and Engineering*, IOP Publishing, 2019.
- [20] M. Foerster, F. Macià, Preface to special issue on magneto-elastic effects, *J. Phys.: Condens. Matter.* 31 (19) (2019) 190301.
- [21] D. Jiles, *Introduction To Magnetism and Magnetic Materials*, CRC Press, 2015.
- [22] X. Liang, C. Dong, H. Chen, et al., A review of thin-film magnetoelastic materials for magnetoelectric applications, *Sensors* 20 (5) (2020) 1532.
- [23] P. Marin, A. Hernando, Applications of amorphous and nanocrystalline magnetic materials, *J. Magn. Magn. Mater.* 215 (2000) 729–734.
- [24] R.C. O'Handley, *Modern Magnetic Materials: Principles and Applications*, Wiley, 2000.
- [25] F.T. Calkins, A.B. Flatau, M.J. Dapino, Overview of magnetostrictive sensor technology, *J. Intell. Mater. Syst. Struct.* 18 (10) (2007) 1057–1066.
- [26] D. Jiles, Theory of the magnetomechanical effect, *J. Phys. D: Appl. Phys.* 28 (8) (1995) 1537.
- [27] M.J. Sablik, D.C. Jiles, Modeling the effects of torsional stress on hysteretic magnetization, *IEEE Trans. Magn.* 35 (1) (1999) 498–504.
- [28] D.C. Jiles, L. Li, A new approach to modeling the magnetomechanical effect, *J. Appl. Phys.* 95 (11) (2004) 7058–7060.
- [29] X. Zhang, M. Zhao, Y. Huang, et al., Novel non-contact torque measurement using the magnetomechanical effect, *Instrum. Sci. Technol.* 47 (1) (2019) 107–116.
- [30] R. Szewczyk, Generalization of the model of magnetoelastic effect: 3D mechanical stress dependence of magnetic permeability tensor in soft magnetic materials, *Materials* 13 (18) (2020) 4070.
- [31] Z. Luo, X. Wei, Analysis of square and circular planar spiral coils in wireless power transfer system for electric vehicles, *IEEE Trans. Ind. Electron.* 65 (1) (2017) 331–341.
- [32] I. Hussain, D.-K. Woo, Simplified mutual inductance calculation of planar spiral coil for wireless power applications, *Sensors* 22 (4) (2022) 1537.
- [33] Z. Zijian, S. Ming, S. Kai, et al., Mutual Inductance Calculation Between Arbitrarily Positioned Polygonal Coils. *Transactions of Nanjing University of Aeronautics & Astronautics*, (S): 120-6.
- [34] H. Tavakkoli, E. Abbaspour-Sani, A. Khalilzadegan, et al., Analytical study of mutual inductance of hexagonal and octagonal spiral planar coils, *Sens. Actuators A: Phys.* 247 (2016) 53–64.
- [35] I.-G. Lee, N. Kim, I.-K. Cho, et al., Design of a patterned soft magnetic structure to reduce magnetic flux leakage of magnetic induction wireless power transfer systems, *IEEE Trans. Electromagn. Compat.* 59 (6) (2017) 1856–1863.
- [36] A. Ostaszewska-Liżewska, M. Nowicki, R. Szewczyk, et al., A FEM-based optimization method for driving frequency of contactless magnetoelastic torque sensors in steel shafts, *Materials* 14 (17) (2021) 4996.
- [37] D.C. Jiles, D.L. Atherton, Theory of ferromagnetic hysteresis, *J. Magn. Magn. Mater.* 61 (1–2) (1986) 48–60.
- [38] H. Sayyaadi, M.R. Zakerzadeh, Position control of shape memory alloy actuator based on the generalized Prandtl-Ishlinskii inverse model, *Mechatronics* 22 (7) (2012) 945–957.
- [39] D. An, H. Li, Y. Xu, et al., Compensation of hysteresis on piezoelectric actuators based on tripartite PI model, *Micromachines* 9 (2) (2018) 44.
- [40] G.-Y. Gu, L.-M. Zhu, C.-Y. Su, Modeling and compensation of asymmetric hysteresis nonlinearity for piezoceramic actuators with a modified Prandtl-Ishlinskii model, *IEEE Trans. Ind. Electron.* 61 (3) (2013) 1583–1595.
- [41] G.-Y. Gu, M.-J. Yang, L.-M. Zhu, Real-time inverse hysteresis compensation of piezoelectric actuators with a modified Prandtl-Ishlinskii model, *Rev. Sci. Instrum.* 83 (6) (2012).
- [42] R. Zhang, Z. Gong, Z. Qiu, et al., Study on stress testing of ferromagnetic materials based on magnetic anisotropy, *Insight, Non-Destr. Test. Cond. Monit.* 64 (1) (2022) 45–49.